

Aggarwal, A. , Pouch, A. M., Lai, E., Lesicko, J., Yushkevich, P. A., Gorman III, J. H., Gorman, R. C. and Sacks, M. S. (2016) In-vivo heterogeneous functional and residual strains in human aortic valve leaflets. *Journal of Biomechanics*, 49(12), pp. 2481-2490.(doi:[10.1016/j.jbiomech.2016.04.038](https://doi.org/10.1016/j.jbiomech.2016.04.038))

This is the author's final accepted version.

There may be differences between this version and the published version. You are advised to consult the publisher's version if you wish to cite from it.

<http://eprints.gla.ac.uk/169777/>

Deposited on: 01 October 2018

Enlighten – Research publications by members of the University of Glasgow
<http://eprints.gla.ac.uk>

In-vivo heterogeneous functional and residual strains in human aortic valve leaflets

*Ankush Aggarwal^{1,2}, Alison M. Pouch³, Eric Lai³, John Lesicko¹, Paul A. Yushkevich⁴,
Joseph H. Gorman III³, Robert C. Gorman³, and Michael S. Sacks¹*

¹Center for Cardiovascular Simulation
Institute for Computational Engineering & Sciences
Department of Biomedical Engineering
The University of Texas at Austin, Austin, TX, USA

²Zienkiewicz Centre for Computational Engineering
Swansea University, Swansea UK

³Gorman Cardiovascular Research Group
Department of Surgery
University of Pennsylvania, Philadelphia, PA, USA

⁴Department of Radiology
University of Pennsylvania, Philadelphia, PA, USA

*Original article to be resubmitted to the Journal of Biomechanics Special Issue “Cardiovascular
Biomechanics in Health and Disease”*

Current: April 26, 2016

For correspondence:

Michael S. Sacks, Ph.D.
W. A. Moncrief, Jr. Simulation-Based Engineering Science Chair I
Institute for Computational Engineering and Sciences
Department of Biomedical Engineering
The University of Texas at Austin
201 East 24th Street, ACES 5.438
1 University Station, C0200
Austin TX 78712-0027 U.S.A.
email: msacks@ices.utexas.edu
Tel: 512-232-7773

Abstract

Residual and physiological functional strains in soft tissues are known to play an important role in modulating organ stress distributions. Yet, no known comprehensive information on residual strains exist, or non-invasive techniques to quantify in-vivo deformations for the aortic valve (AV) leaflets. Herein we present a completely non-invasive approach for determining heterogeneous strains – both functional and residual – in semilunar valves and apply it to normal human AV leaflets. Transesophageal 3D echocardiographic (3DE) images of the AV were acquired from open-heart transplant patients, with each AV leaflet excised after heart explant and then imaged in a flattened configuration ex-vivo. Using an established spline parameterization of both 3DE segmentations and digitized ex-vivo images (Aggarwal et al., 2014), surface strains were calculated for deformation between the ex-vivo and three in-vivo configurations: fully open, just-coapted, and fully-loaded. Results indicated that leaflet area increased by an average of 20% from the ex-vivo to in-vivo open states, with a highly heterogeneous strain field. The increase in area from open to just-coapted state was the highest at an average of 25%, while that from just-coapted to fully-loaded remained almost unaltered. Going from the ex-vivo to in-vivo mid-systole configurations, the leaflet area near the basal attachment shrank slightly, whereas the free edge expanded by ~10%. This was accompanied by a 10° - 20° shear along the circumferential-radial direction. Moreover, the principal stretches aligned approximately with the circumferential and radial directions for all cases, with the highest stretch being along the radial direction. Collectively, these results indicated that even though the AV did not support any measurable pressure gradient in the just-coapted state, the leaflets were significantly pre-strained with respect to the excised state. Furthermore, the collagen fibers of the leaflet were almost fully recruited in the just-coapted state, making the leaflet very stiff with marginal deformation under full pressure. Lastly, the deformation was always higher in the radial direction and lower along the circumferential one, the latter direction made stiffer by the preferential alignment of collagen fibers. These results provide significant insight into the distribution of residual strains and the in-vivo strains encountered during valve opening and closing in AV leaflets, and will form an important component of the tool that can evaluate valve's functional properties in a non-invasive manner.

Keywords: Heart valves, aortic valve, valve mechanics, residual strains, in-vivo analysis

1 Introduction

In biosolid mechanics, the presence of tissue stress levels that maintain high level of uniformity without stress concentrations has long been considered closely related to maintenance of tissue homeostasis, with deviations from the homeostatic state seen as a secondary feature to various pathologies (Chuong and Fung, 1986a, b; Fung, 1991). Thus, changes in the associated tissue deformation patterns from those normally experienced due to various pathologies in-vivo may lead to altered cellular responses and tissue remodeling linked with efforts to restore pre-existing normal stress states. Moreover, critical linkages to the underlying valve interstitial cell mechanobiological responses (Sacks et al., 2009) require a detailed knowledge of the relation between tissue and cellular deformation (Lee et al., 2015), which is only possible when the in-vivo strain and stress states are accurately known. Thus, the knowledge of accurate residual strains in heart valves is critical to elucidating their function.

Yet, the level and functional role of residual strains in heart valves remains an open issue, and poses questions such as whether the native valve leaflets are pre-strained in their native environment and how this evolves during growth and disease. Interestingly, if pre-strains exists then *none* of the configurations of the heart valve is stress-free in-vivo, necessitating excision of leaflets for identification of true stress-free state. Moreover, accounting for these residual strains has been shown to be extremely important in in-vivo stress estimations, as it leads to order of magnitude differences in the estimated valve tissue stiffness (Rausch and Kuhl, 2013). While it is anticipated that some level of residual strains exists in all heart valves, this has not been verified or quantified other than for the mitral valve (MV) (Amini et al., 2012). In that study, physical markers were used, limiting its clinical applicability, as well as restricting the calculated strains to a sub-region of the leaflet. Thus, the need for valve excision and physical markers in determination of residual strains has rendered it challenging to perform such studies in healthy human subjects. While residual strains are known to exist within the aortic valve (AV) layers (Stella and Sacks, 2007; Vesely et al., 1993; Vesely and Noseworthy, 1992), it is yet to be determined if residual strain exist in the AV tissues in the in-vivo state.

Clearly, it is necessary to quantify both in-vivo and excised states in order to determine heart valve residual and functional strain fields. Alternative approaches have been developed that partly allow determination of the unloaded configurations in vascular structures using inverse approaches (Lu et al., 2007; Rajagopal et al., 2007). However, these are restricted to removing stresses induced by external loads and cannot determine the residual strains caused by incompatibilities in structural components or displacement boundary conditions. Others have proposed novel elasticity or constitutive frameworks for residually stressed structures (Gower et al., 2015; Johnson and Hoger, 1995; Lu, 2012). However, these are difficult to implement for non-linear and anisotropic material behavior in anatomical structures. Recent efforts have made progress towards in-vivo analysis of heart valves (Krishnamurthy et al., 2008; Lee and Sacks, 2014; Rausch and Kuhl, 2013). However, most of these methods employed some physical markers to obtain the strain field limiting their clinical usability. There are no suitable methods for determining the in-vivo strains experienced by heart valves in a non-invasive manner.

In this work, we present a technique for determining in-vivo heterogeneous surface strains for semilunar valve leaflets without the need of physical markers, and apply it to healthy human AV. We used latest transesophageal 3D echocardiographic (3DE) imaging technology and segmentation algorithm for determining the in-vivo AV geometry. Utilizing data from heart transplant patients with healthy AV, we excised the leaflets and imaged them ex-vivo. Applying our novel marker-less technique to both 3DE segmentations and digitized ex-vivo images, we calculated the deformation of the valve leaflets between the in-vivo and ex-vivo states, using the following three in-vivo configurations: open, just-coapted and fully-loaded. This allowed us to quantify the resulting heterogeneous deformations over the entire leaflet during cardiac cycle and relate them to the local fiber architecture.

2 Methods

The complete analysis started by selecting patients who underwent ultrasound immediately before their heart transplant. The AV leaflets were excised from the transplanted hearts, followed by analysis of in-vivo and ex-vivo images of those leaflets (Fig. 1). In-vivo analysis constituted image segmentation and processing, and ex-vivo analysis produced shape and fiber structure of excised flattened leaflets. For each image, both in-vivo and ex-vivo, a spline surface representation was obtained and using the spline parameterization strains were calculated between various valve states.

2.1 Patient selection

Patients were included in the study after University of Pennsylvania Institutional Review Board approval and obtaining informed consent. All of the patients had trileaflet AV that were classified as minimally calcified based on echocardiography and direct observation (Table 1). Data was utilized from only those heart transplant patients that produced adequate echocardiography image quality. In addition, patients with prior AV surgery, history of endocarditis, rheumatic fever, congenital heart defects, and chronic inflammatory disease were excluded.

2.2 Image acquisition

Transesophageal 3D echocardiographic (3DE) images of the AV were acquired from each heart transplant patient. The images were obtained with the iE33 platform (Philips Medical Systems, Andover, MA) using a 2 to 7 MHz matrix-array transducer. For each subject, 3DE images were selected at three time points in the cardiac cycle: the just-coapted state (zero transvalvular pressure), the fully-loaded state (maximum transvalvular pressure), and the open state (at mid-systole). These images were exported in Cartesian format with an approximate size of 224 x 208 x 208 voxels and nearly isotropic resolution of 0.4 to 0.8 mm.

2.3 Specimen collection

AV leaflets were excised after explantation of the heart, with leaflets in the right, left, and non-coronary sinus positions randomly selected from each patient. Excised leaflets were labeled with the sinus

position and placed in 1x phosphate buffered saline (Sigma-Aldrich, St. Louis, MO). The leaflets were transferred overnight (in less than 24 hours) on ice to the University of Texas Austin.

2.4 *Ex-vivo determination of fiber orientation and shape and size of explanted leaflets*

After receiving the leaflets, the samples were laid flat and fixed with 0.5% aqueous glutaraldehyde for 4 hours. In total, all samples were tested within 29 hours of the explant. Two-dimensional images were taken of the flattened leaflets, and then prepared for collagen fiber architecture (CFA) measurements using small angle light scattering technique (Sacks et al., 2004; Sacks et al., 1997) to obtain the preferred fiber directions N_1 . This state of AV leaflet in rest of the analysis is termed as the ex-vivo state, signifying the configuration once the leaflets have been excised.

2.5 *Image analysis*

2.5.1 *3DE image segmentation*

For each subject, segmentation of the AV apparatus was performed firstly in the open state (systole) using a multi-atlas segmentation and deformable modeling technique described in Pouch et al. (2015b). Although different cusps were excised from each heart, segmentation of the entire AV apparatus was performed for all subjects. The segmentations included five labels as described in Nomenclature (Table 2). The process of segmenting a 3DE image of the open AV is summarized as follows (Fig. 2a):

- *Manual landmarking*: Five landmarks were manually identified in the 3DE image of the AV (Table 2). These landmarks ensured accurate initialization of multi-atlas segmentation.
- *Multi-atlas segmentation*: The 3DE image was segmented using multi-atlas label fusion, a technique that assigns anatomical labels to each voxel in the 3DE image by combining information from a set of manually traced 3DE images (Hongzhi et al., 2013). In this work, the atlas set consisted of fifteen 3DE images of normal adult AV at systole that had been manually traced in ITK-SNAP (Yushkevich et al., 2006b).
- *Deformable modeling*: A model of the open AV, which in turn was based on 3DE data of patients not included in this study, was deformed to capture the geometry of the aortic leaflet surfaces in the multi-atlas segmentation result (Pouch et al., 2015c). The deformable model used here was a continuous medial axis representation (Yushkevich et al., 2006a), which enabled the extraction of a medial surface of each aortic cusp (i.e. a surface between the ventricular and aortic surfaces). Once obtained, a triangulated medial surface of each leaflet was generated.

In order to generate segmentations of the AV at the just-coapted state, diffeomorphic registration (Avants et al., 2008) was used to determine a transformation that maps the 3DE image of the open AV to the 3DE image of the just-coapted valve within the same image series. The resulting deformation fields were used to transform the segmentation of the open valve to the just-coapted state. Likewise, the just-coapted segmentation was transformed to the fully-loaded state using deformable image registration. Finally, a deformable template was fitted to the just-coapted and fully-loaded segmentation results, and triangulated meshes of the medial surfaces of the cusps were extracted from the fitted models, comprised of roughly 30 nodes and 40 triangles. In this work, two templates were used: an open template for the unloaded AV and a closed template for the just-coapted and fully loaded AV. The rationale for using separate templates is

that leaflet geometry is more accurately captured when a template in the same state as the target segmentation is used.

2.5.2 Digitization of ex-vivo 2D images

In 2D images of leaflets, the background produces an isotropic scattering pattern. This property was used to differentiate the tissue area from the background and digitize it. The tissue points were converted to a mesh of square elements – each square represented the point of measurement and contained fiber direction. Leaflet edges were extracted based on node connectivity using Paraview (Squillacote).

2.5.3 Analysis of 2D and 3D images

In order to find the mapping between various leaflet configurations obtained from segmentation/digitization and, in turn, evaluate the corresponding strains, the leaflet shapes were parameterized using a common set of coordinates via 2D splines. A spline fitting technique previously developed (Aggarwal et al., 2014) was used to obtain parameterized coordinates for all points in a given leaflet configuration (Fig. 2b). The segmented/digitized surface was defined using n points $\mathbf{x}_i \in \mathbb{R}^3$ where $(i=1\dots n)$ and these points together constituted a two-dimensional surface \mathfrak{M} in the three dimensional space. The parameter space for a 2D spline surface was $\mathfrak{U} = [0,1] \otimes [0,1]$, so that fitting a spline surface to the leaflet provided us with a mapping $s : \mathfrak{U} \rightarrow \mathfrak{M}$. Therefore, we had a point to point mapping $\mathbf{u}_i \rightarrow \mathbf{x}_i$, where $\mathbf{u}_i \in \mathfrak{U} \subset \mathbb{R}^2$ as well as a mapping from any point $\mathbf{u} \rightarrow \mathbf{x}$ where $\mathbf{u} \in \mathfrak{U}$ and $\mathbf{x} \in \mathfrak{M}$. The steps involved in obtaining the mapping $s : \mathfrak{U} \rightarrow \mathfrak{M}$ are provided in the Appendix A.1 for completeness.

2.6 Calculation of strain

Given two configurations of a leaflet \mathfrak{M}^a and \mathfrak{M}^b , spline surface fitting was performed to obtain mapping between the common parameter space and each of those two configurations $s^a : \mathfrak{U} \rightarrow \mathfrak{M}^a$ and $s^b : \mathfrak{U} \rightarrow \mathfrak{M}^b$. In principle, we could obtain the mapping from configuration a to b by evaluating $(s^a)^{-1} \cdot s^b$, and then the associated strains. However, we note that there were small errors associated with these mappings, which might amplify while calculating the strains because of the derivatives involved. Therefore, we used a finite number of points $\bar{\mathbf{u}}_j \in \mathfrak{U}$, $j=1\dots p$ to calculate the corresponding mapped points in two configurations, that is $s^a : \bar{\mathbf{u}}_j \rightarrow \bar{\mathbf{x}}_j^a$ and $s^b : \bar{\mathbf{u}}_j \rightarrow \bar{\mathbf{x}}_j^b$. Since we match the boundary and commissure points exactly, and $\bar{\mathbf{x}}_j^a$ and $\bar{\mathbf{x}}_j^b$ have the same parametric coordinates $\bar{\mathbf{u}}_j$, they represented approximately the same *material points* in the leaflet. Based on our previous study (Aggarwal et al., 2014), we used these p points and their triangulation to calculate strains. Using linear shape functions for triangular finite elements, we calculated the deformation gradient tensor \mathbf{F}_a^b from state a to b , at the centroid of each triangle (for details of deformation gradient calculation, see Appendix A.2). In the calculations that follow, we used number of points $p=14$, which included 2 commissure points, 3 on the free edge, 5 on the basal attachment

and 4 on the interior of leaflet surface (Fig. 2c). These points, which we treated as “virtual markers”, were placed symmetrically over the leaflet. Using 14 points, we obtained 16 triangular elements; since linear shape function gives constant strain, we calculated 16 deformation gradient tensors for each mapping (Fig. 2c).

The stretch vectors were calculated using eigenvalue decomposition of Cauchy-Green tensor $\mathbf{c} = \mathbf{F}^T \mathbf{F}$. Since we are only concerned with planar strains, the eigenvectors directed along the triangle normal in configuration \mathfrak{a} was ignored. The square root of the other two eigenvalues provided the two principal stretches λ_1 and λ_2 . In the direction with unit vector \mathbf{N} , stretch ratio was calculated using $\sqrt{\mathbf{N} \cdot \mathbf{c} \cdot \mathbf{N}}$. Since fibers in AV are predominantly aligned along the circumferential direction, the stretches were calculated along and perpendicular to the fibers using circumferential and radial directions respectively. The average stretch over all the samples was mapped and represented on the average AV leaflet shape calculated previously (Aggarwal et al., 2014). Given two directions \mathbf{N}_1^a and \mathbf{N}_2^a in the configuration \mathfrak{a} , the change in angle during deformation $\mathfrak{a} \rightarrow \mathfrak{b}$ represents shear and is given by

$$\Delta \theta_{1,2} = \cos^{-1} \left(\frac{\mathbf{N}_1^a \cdot \mathbf{N}_2^a}{|\mathbf{N}_1^a| |\mathbf{N}_2^a|} \right) - \cos^{-1} \left(\frac{(\mathbf{F}_a^b \cdot \mathbf{N}_1^a) \cdot (\mathbf{F}_a^b \cdot \mathbf{N}_2^a)}{|\mathbf{F}_a^b \cdot \mathbf{N}_1^a| |\mathbf{F}_a^b \cdot \mathbf{N}_2^a|} \right), \quad (1)$$

where $|\cdot|$ is the magnitude of vector. Shear angle was calculated along the circumferential-radial (CR) direction. Lastly, $J = \lambda_1 \lambda_2$ was used to represent the leaflet area dilatation within each triangle.

2.7 Statistical analysis

In order to improve the statistical sampling, results from all three AV leaflet types – left coronary, right coronary, and non-coronary – were pooled (Table 3). For the overall geometrical measurements, such as the total leaflet area and lengths of the free edge and basal attachment, the results were averaged. Furthermore, for regional analysis, the leaflets were assumed to follow symmetric deformation patterns, which doubled the sample sizes. The variations in all calculated variables were represented using standard deviation (SD) and standard error of mean (SEM). Welch's t-test was performed to establish significance of changes in overall leaflet kinematics from one state to another. For establishing significance of regional differences in strain measures, paired t-test was performed to obtain a p value for each pair of regions.

3 Results

3.1 Leaflet reconstructions, areal and dimensional metrics.

As in our previous studies (Aggarwal et al., 2013; Aggarwal et al., 2014), the 3DE segmentation and spline representations provided an excellent fit to the raw leaflet data (Figs. 3, 4). Mean errors using the surface normal error were ± 0.2 mm, very similar to our previous study using in-vitro data (Aggarwal et al., 2014). From the reconstructions, we firstly determined the average leaflet areas and the free edge and basal

attachment lengths. Results indicated that total leaflet areas increased monotonically from ex-vivo to the fully-loaded state (Fig. 5-a, Table 4). Proportional changes in area indicated a nearly 30% increase from the ex-vivo to open state, indicating substantial pre-strain of the leaflet tissue (Fig. 5-b). This also manifested in the proportional changes between fully loaded/open (~27% increase) vs. fully loaded/ex-vivo (~64% increase) (Fig. 5-b). In contrast, the length of the basal attachment remained nearly constant at ~42 mm, whereas the free edge increased from ~25 mm ex-vivo to ~30 mm in-vivo (Fig. 5c).

After sub-dividing the leaflet half into eight triangular regions, the local area changes varied markedly both over the leaflet (Fig. 6). Interestingly, the average area change was positive everywhere, however it was highest near the commissure. For the ex-vivo to in-vivo closed state, the leaflet area, on an average, expanded in the range of 30–100%. When referenced to the open state, this range was reduced to 5–65%. There was some variation across samples, which was slightly higher near the commissure and for the ex-vivo to in-vivo deformation. Collectively, these results suggest a substantial regional variation and pre-strain of the AV leaflet.

3.2 *Stretch ratios*

The principal stretches for all the mappings were approximately aligned with the circumferential and radial directions, with higher stretches acting radially (Fig. 7). For the ex-vivo to in-vivo open state, the leaflet experienced high stretches in the radial direction, with the circumferential stretch close to one. In contrast, the radial stretch varied widely in regions. There was no radial stretch in the basal area, while other areas experienced a significantly different stretch of 25-50% (Table 5). Comparing different areas, the variation was relatively higher near the commissure. Whereas, comparing deformation between various states, the variation was highest for the ex-vivo to in-vivo deformation. For the just-coapted to fully-loaded deformation, the circumferential stretch was close to one over most of the leaflet, except near the commissure and basal region. In those two regions, the leaflet stretched by 15% in the fiber preferred direction. For the leaflet deformation from open to just-coapted state, the maximum stretch was in 1.3-1.7 range (Fig. 7) and the circumferential principal stretch varied much less and was within the 0.8-1 range, representing local contraction. The stretch ratio along the circumferential direction was slightly higher than one, except near the commissure where it was approximately 1.3-1.5. Regional cumulative deformations from ex-vivo to fully-loaded state showed similar trends, where the principal stretches were aligned with the circumferential and radial directions (Fig. 8). The average stretch in the circumferential direction was close to one for all regions, whereas the radial direction experienced an approximately 50% stretch. The deformation from open to closed state showed different pattern (Fig. 9). The circumferential stretch was close to one for all regions except near the commissure. Whereas, the leaflets stretched by roughly 25-50% in the radial direction with higher values observed in the interior of the leaflet. Furthermore, in the coaptation region, the principal stretches deviated from the radial direction slightly.

3.3 Shear angle

For both the just-coapted to fully-loaded and open to just-coapted mappings, the shear was approximately 10-20° at all points except near the commissure where it was higher at nearly 28°. For the ex-vivo to in-vivo open state, the CR shear was also in the range of 10-20°, whereas the maximum shear was much higher reaching more than 40° near the commissure. The variations across samples were similar for all the cases, but slightly higher for the ex-vivo to in-vivo measurement. Even for the cumulative deformations, the shear in the interior of the leaflet along CR direction was in 10-20° range, whereas the maximum shear was in 20-30° range (Fig. 10). Interestingly, it was lower in the coaptation region for ex-vivo to fully-loaded deformation, and was higher near the commissures for open to closed state deformation.

4 Discussion

4.1 Presence of residual strains in biological structures

In spite of their importance, investigation into the residual strains in heart valves is relatively new (Aggarwal et al., 2013; Amini et al., 2012; Rausch et al., 2013; Rausch and Kuhl, 2013). This is partly because of the significant difficulty in obtaining the in-vivo images and segmentation of the leaflet geometry, as well as matching excised leaflets. In the present work, we utilized the latest imaging and segmentation technology and a novel technique to measure strains in AV leaflets that provided a heterogeneous strain field without the need of physical markers. To the best of the authors' knowledge, this was the first attempt to measure residual strains in healthy human AV leaflets. In addition to residual strains, we also calculated the strains experienced in-vivo during valve closure starting with the open state and deforming successively to just-coapted and fully-loaded states. We found that the leaflet area increased by approximately 25% as the valve closed from mid-systole to just-coapted state, even though the valve was not yet supporting any pressure difference. The change in linear dimensions of the leaflets (the free edge and basal attachment lengths) under this deformation was limited to only 3-5%. A heterogeneous analysis revealed that the local area change was highly non-uniform, ranging from almost no change in some parts to more than 50% increase in others. Furthermore, a 20% area increase was associated with the deformation from ex-vivo to in-vivo open state. Conversely, the AV leaflets shrank by an average of 17% upon excision; however, the change in linear dimensions was much smaller. Interestingly, even though the free edge shrank upon excision, the basal attachment expanded slightly as the residual stress was released. This led to a highly non-uniform strain distribution with some areas experiencing small shear and other experiencing larger one.

For almost all of the cases, the maximum stretch was aligned to the radial direction (Fig. 7). This was expected as the collagen fibers run predominantly along the circumferential direction. The resulting strains near the commissure were relatively more variable across samples compared to other areas of the leaflet. Since we used boundary to calculate the strains, the commissure region will receive geometric contributions from both free edge and basal attachment. This might lead to a high variability in the commissure strains as observed here and will need a more thorough error analysis of the mapping

technique. However, in general the results presented here are in good agreement with previous studies. For example, the radial stretches have been reported to be higher than the circumferential ones in porcine valves (Adamczyk et al., 2000; Weiler et al., 2011), with values of strains in the same range as our presented results. However, a direct comparison of strain values is not possible. For example, in Weiler et al. (2011), porcine AV was studied in-vitro without addressing the residual strains, whereas current study is focused on human AV in-vivo. Varied strains observed here in the coaptation region and near the commissure are also consistent with the microstructural variations reported in AV (Aggarwal et al., 2014). Use of normal human samples in this study and their non-invasive in-vivo analysis allows us to make inferences about the functional behavior of the AV.

4.2 *Functional implications*

The presented results provide unique information about residual strains existing in human AV leaflets and the strains experienced during healthy valve closure. During the leaflet deformation from just-coapted to fully-loaded, the area change was minimal and circumferential stretch was close to one over most of the leaflet. This indicates that most of the collagen fibers were already recruited in the just-coapted state, making the circumferential direction highly stiff. Analyzing the cumulative deformations, we observed roughly 50-100% area increase over most of the leaflet with higher strains near the commissures and lower strains in the coaptation zone. These results are consistent as the region near commissures experiences the highest stress concentrations and the coaptation area is where leaflets come in contact. Additionally, the circumferential direction always showed significantly smaller strains compared to the radial one. Collectively, these results indicate that by the time leaflet starts supporting pressure difference, the collagen fibers had already recruited and stiffened resulting in very high stiffness. In our previous study of AV (Stella and Sacks, 2007), we have found approximately 50% increase in area from unloaded to physiological stress levels. This suggests that the residual strains reported in the present study effectively cover the “toe” region of the AV stress-strain behavior (Adamczyk et al., 2000; Doebling et al., 2005; Stella and Sacks, 2007). Functionally, this suggests that it is the elastin fibers in the ventricularis layer that produce the leaflet pre-stress, and that remaining physiological stress-strain behavior is determined by the collagen fiber network. Moreover, the anisotropic residual strains are likely a result of both the orientations of the collagen and elastin networks and their large rotations, rather than a single fiber population.

4.3 *Limitations*

Accuracy of the entire method is based on the quality of the in-vivo reconstruction and the spline fitting technique. For the former, we note that it has been extensively validated and known to produce accurate results when compared to the manual segmentation (Jassar et al., 2014; Pouch et al., 2015b; Pouch et al., 2013; Witschey et al., 2014). For the later, we have extensively validated the method against gold-standard in-vitro data with accuracies to ± 0.2 mm (Aggarwal et al., 2014). Yet, even these small errors in spline fitting method limited the extent of heterogeneity we could capture to 16 sub-regions each with a homogeneous strain. For obtaining a continuous strain field, further improvements would be needed in the

algorithm to reduce the fitting error. We note too that some “apparent” leaflet shortening may take place because of the flattening of tissue during ex-vivo analysis, whereas it has an intrinsic curvature in-vivo. This effect has been shown to be small, and, therefore, we did not account for it in the present study. Although sufficient for this study, the size of the sample dataset will have to be expanded to establish trends between three leaflet types and analyze the asymmetry of leaflet strains. The 3DE frames chosen to represent the various states had a time resolution of approximately 50 msec and, thus, were not exactly contemporaneous. Because of the quick opening/closing behavior of the valve, this becomes especially important for the just-coapted state.

4.4 Conclusions and future work.

We presented a framework for calculating heterogeneous strains in valve leaflets and applied it to healthy human AV samples. Using advanced 3DE segmentation technology and marker-free method, we calculated the strains AV leaflets experience in-vivo as well as the residual strains related to excision. We observed clear trends in the deformation behavior of AV leaflets, and the strains were found to be heterogeneous and anisotropic. The regional variations in strain and its relationship with the preferred direction of collagen fibers provided important functional insights into AV leaflets’ in-vivo behavior. The results also demonstrated a “locking-type” behavior of valve leaflets where they become highly stiff as they start supporting pressure difference, which could be a driving force behind residual strain development. Main strength of the presented framework is the marker-less approach and its capability to describe heterogeneous strains over entire leaflet. These results will form the basis of the critical information needed for accurately modeling and predicting biomechanical properties of the healthy human aortic valve leaflets in a non-invasive manner (Aggarwal and Sacks, 2015a; Aggarwal and Sacks, 2015b).

In the future, we will apply this framework to pulmonary valve, as well as pathological valves like the bicuspid aortic valve. It will allow us to determine any differences between various healthy and diseased valves. We would also work on improving the spline-based technique and reduce the errors associated such that it can be used to obtain a continuously varying strain field over the leaflet surface. The strains calculated in this study will be combined with the inverse modeling tool we developed previously to obtain more accurate estimate of biomechanical properties of the heart valve leaflets (Aggarwal and Sacks, 2015b).

Acknowledgements: This work was supported by the American Heart Association (Grant No. 14POST18720037 to A.A.), Welsh Government and Higher Education Funding Council for Wales through the Sêr Cymru National Research Network in Advanced Engineering and Materials (Grant No. F28 to A.A.), and National Institutes of Health (Grant No. R01 HL108330 to M.S.S).

Conflict of Interest: The authors declare that they have no conflict of interest.

A Appendices

A.1 Spline fitting

The methods used here was taken from a previous in-vitro study (Aggarwal et al., 2014). We start with a two dimensional manifold \mathfrak{M} embedded in three-dimensional space \mathbb{R}^3 . The surface initially is defined using n points $\mathbf{x}_i \in \mathbb{R}^3$ where $i=1 \dots n$. We want to fit a spline surface to it with parametric coordinates $\mathfrak{U} = [0,1] \otimes [0,1]$. Therefore, the problem is to determine the mapping $s : \mathfrak{U} \rightarrow \mathfrak{M}$. Assume that we have a starting spline surface (an initial guess), so for fitting it to the point cloud \mathbf{x}_i we minimize the norm of the distance between point cloud and its projection on the spline surface \mathbf{x}_i^p to determine the control points \mathbf{c}_j

$$\min_{\mathbf{c}_j} \sum_{i=1}^n \left| \mathbf{x}_i - \mathbf{x}_i^p \right|^2 = \min_{\mathbf{c}_j} \sum_{i=1}^n \left| \mathbf{x}_i - \sum_j N_j(\mathbf{u}_i^p) \mathbf{c}_j \right|^2 = \min \left| \mathbf{x} - \mathbf{A} \mathbf{c} \right|^2 \quad (\text{A.1})$$

Here, \mathbf{c} is a vector of the control points \mathbf{c}_j and \mathbf{A} is the matrix of shape functions with $A(i, j) = N_j(\mathbf{u}_i^p)$. The shape functions $N_j(\mathbf{u})$ in one dimension are calculated recursively starting from step function and those in higher dimensions are calculated via tensor product. The minimization problem Eq. (A.1) can be easily shown to be equivalent to solving a linear system $\mathbf{c} = (\mathbf{A}^T \mathbf{A})^{-1} \mathbf{A}^T \mathbf{x}$. The projection point \mathbf{x}_i^p and the corresponding parametric coordinates \mathbf{u}_i^p are calculated using normality condition that was solved numerically with Newton's method.

However, there are two problems in the above method. 1) It is hard to obtain a good initial guess. 2) More importantly, as it is, this method leads to large oscillations at the boundary. Therefore, the problem was solved in two steps.

1. A one dimensional spline curve was fit to the boundary of surface $\partial \mathfrak{M}$ which was converted into a two dimensional spline surface
2. Using this spline surface as the initial guess and keeping the boundary control points fixed, it was fit to the surface \mathfrak{M}

Some modifications had to be made so that one can convert a spline curve into a spline surface. Since we are approximating a semi-lunar shape as a spline surface, we restrict that the 2D spline has degenerate points at the boundary of first parametric coordinate (Fig. 2b). Accordingly, the 1D spline is a closed curve and C2-continuous with two C⁰-continuous points. Lastly, these two sections of this 1D spline must have the same knot vector. Therefore, in summary the steps involved in this spline-fitting algorithm are:

1. Initialize a closed C²-continuous spline curve with two C⁰-continuous points
 - a. Iteratively solve equation A.1 updating the projection point at every iteration

- b. Refine the spline using knot insertion and go to previous sub-step – perform until a good fit is obtained
2. Convert the curve to a spline surface which will serve as the initial guess
 - a. Iteratively solve equation A.1 updating the projection point at every iteration and keeping the boundary control points fixed
 - b. Refine the spline using and go to previous sub-step – perform until a good fit is obtained

A.2 Deformation gradient calculation

To derive the deformation gradient mathematically, let us say the point $\bar{\mathbf{x}} = (x, y, z)$ and we use parametric coordinates in linear finite elements ξ and η . Further, if three vertices of a triangular element are $\bar{\mathbf{x}}_j^a$, $\bar{\mathbf{x}}_k^a$ and $\bar{\mathbf{x}}_l^a$, then we have the relations:

$$\begin{aligned}
 x^a &= x_j^a + (x_k^a - x_j^a)\xi + (x_l^a - x_j^a)\eta \\
 y^a &= y_j^a + (y_k^a - y_j^a)\xi + (y_l^a - y_j^a)\eta \\
 z^a &= z_j^a + (z_k^a - z_j^a)\xi + (z_l^a - z_j^a)\eta
 \end{aligned} \tag{A.2}$$

Similarly, we would have the relations for state b. Therefore, the deformation gradient from a to b is

$$\mathbf{F}_a^b = \begin{bmatrix} \frac{\partial x^b}{\partial \xi} & \frac{\partial x^b}{\partial \eta} & n_x^b \\ \frac{\partial y^b}{\partial \xi} & \frac{\partial y^b}{\partial \eta} & n_y^b \\ \frac{\partial z^b}{\partial \xi} & \frac{\partial z^b}{\partial \eta} & n_z^b \end{bmatrix} \begin{bmatrix} \frac{\partial x^a}{\partial \xi} & \frac{\partial x^a}{\partial \eta} & n_x^a \\ \frac{\partial y^a}{\partial \xi} & \frac{\partial y^a}{\partial \eta} & n_y^a \\ \frac{\partial z^a}{\partial \xi} & \frac{\partial z^a}{\partial \eta} & n_z^a \end{bmatrix}^{-1}, \tag{A.3}$$

Where, n_x^a , n_y^a and n_z^a are three components of the triangle normal vector in configuration a and

correspondingly in b. The Green-Lagrange strain is then calculated as $\mathbf{E} = \frac{1}{2}(\mathbf{F}^T \mathbf{F} - \mathbf{I})$.

TABLES

Table 1. Patient Characteristics

Number of Patients	5
Age (years)	63±3
Male	3 (0.60)
BMI (kg/m ²)	29.3±4.7
NYHA	3
Hypertension	4 (0.80)
Hyperlipidemia	3 (0.60)
Coronary Artery Disease	3 (0.60)
Chronic Kidney Disease	1 (0.20)
Diabetes mellitus	2 (0.40)

NYHA, New York Heart Association; BMI, Body Mass Index

Table 2: Nomenclature used in describing the 3DE image segmentation process

Segmentation	A 3D image of labels corresponding to the aortic valve apparatus in a 3DE grayscale image
Label	A number assigned to each voxel in an image indicating its membership to an anatomical structure. The following labels were used in the aortic valve segmentation: 0 – background, 1 – left coronary cusp, 2 – non-coronary cusp, 3 – right coronary cusp, 4 – sinus segment, 5 – ventricular outflow segment (Fig. 2a)
Landmark	An anatomically relevant point in an image. The landmarks used to initialize 3DE image segmentation in this study included the three commissures, the center of the outflow tract at the level of the left ventricular outlet, and the center of the outflow tract at the level of the sinotubular junction
Atlas	A 3DE grayscale image and its manual segmentation

Table 3: Summary of sample sizes of various maps

Mapping Case	#LC	#RC	#NC	#Total
Ex-vivo to mid-systole	3	3	1	6
Mid-systole to just-coapted	3	4	2	9
Just-coapted to fully-loaded	3	4	2	9
Ex-vivo to fully-loaded	2	3	1	6
Mid-systole to fully-loaded	3	4	2	9

Table 4: Leaflet areas of aortic valve at three different configurations

Sample #	Leaflet	Leaflet areas (cm ²)			
		Ex-vivo	Mid-systole	Just-coapted	Fully-loaded
1	LC	-	2.87	3.60	3.78
	RC	-	3.77	4.07	3.74
	NC	-	3.39	4.43	4.65
2	LC	2.08	2.14	3.05	3.38
	RC	2.33	3.48	4.29	4.75
3	LC	2.07	-	2.65	-
	NC	1.88	-	2.67	-
4	LC	3.15	3.00	4.15	4.08
	RC	2.57	3.50	3.91	3.85
5	RC	2.45	2.73	3.20	3.17
	NC	1.98	2.20	2.73	2.83
<i>n</i>	All	8	9	11	9
Average±SD	All	2.32±0.39	3.00±0.55	3.52±0.65	3.8±0.60

Table 5: Significant regional variations in kinematic measures (p<0.05)

Area change	Ex-vivo → closed	D2 < D1
	Open → closed	B1 < A1, B2, D1
		D2 > C
Circumferential stretch	Ex-vivo → open	D1 > D2
	Open → Just coapted	A1 > B2, C, D
		A2 > D
	Just coapted → Closed	A1 > C1
	Ex-vivo → Closed	A2 > A1, B2, C, D
		D2 < D1, C2
	Open → Closed	A1 > B, C, D
		A2 > B, C
Radial stretch	Ex-vivo → open	D2 < A, B, C, D1
	Open → just coapted	C1 > A2
		D1 > A2, B, C2
		D2 > A, B, C, D1
	Just coapted → closed	A1 > B2, D
		A2 > D
		B1 > B2, D2
	Ex-vivo → closed	D1 > C2, D2
	Open → closed	A2 < C1
		D2 > A, B1, C2, D1

Figure captions

Figure 1 – Flow chart of the study showing Overall methods involved patient selection, ultrasound, leaflet excision for ex-vivo analysis, segmentation, spline-fitting, and strain analysis

Figure 2 – (a) Schematic of aortic valve segmentation and modeling, with the segmentation labels shown in color (*adapted from (Pouch et al., 2015a)*). (b) The parameter mapping from spline space to the leaflet surface and “virtual” markers and region definitions for strain calculation. (c) The average leaflet template symmetrically divided into 16 triangular regions.

Figure 3 - Example segmentations and spline fitting at open (mid-systole) configuration. Also shown are two views of the segmentations and spline fitting, the latter showing very close agreement.

Figure 4 - Example segmentations and spline fitting at fully loaded configuration. Also shown are two views of the segmentations and spline fitting, the latter showing very close agreement.

Figure 5 - Area and key linear dimensions of the entire leaflet for all the leaflets, showing (a) averaged areas, (b) area ratios, and (c) free edge length and basal attachment length for all four states. (Number of samples are provided in Tables 3 and 4, and error bars indicate SEM, * $p < 0.05$)

Figure 6 - Areal strain invariant J for local deformation of leaflets at different points – A1, A2, B1, B2, C1, C2, D1, and D2. (Number of samples are provided in Table 3 and error bars indicate SEM)

Figure 7 – Mapping of circumferential and radial stretches for all five transitions states considered averaged over all samples. Substantial regional variations were observed in all configurations, with the radial direction consistently larger in most cases. Interestingly, the basal regions (lowest two regions) reveal no deformations from the ex-vivo to the in-vivo states

Figure 8 – Regional variations in circumferential and radial stretches in the ex-vivo to open, open to just coapted, and just-coapted to closed states. (Number of samples are provided in Table 3 and error bars indicate SEM)

Figure 9 – Regional variations in circumferential and radial stretches in the ex-vivo to closed and open to closed states. For all regions, substantial pre-strains were observed. Moreover, when referenced to the open state, the commissure regions revealed a substantially larger circumferential stretch compared to the radial stretch. (Number of samples are provided in Table 3 and error bars indicate SEM)

Figure 10 – Regional shear values for the ex-vivo to closed and open to closed states. Most shearing angles were modest, and in the range of 10 to 15 degrees. (Number of samples are provided in Table 3 and error bars indicate SEM)

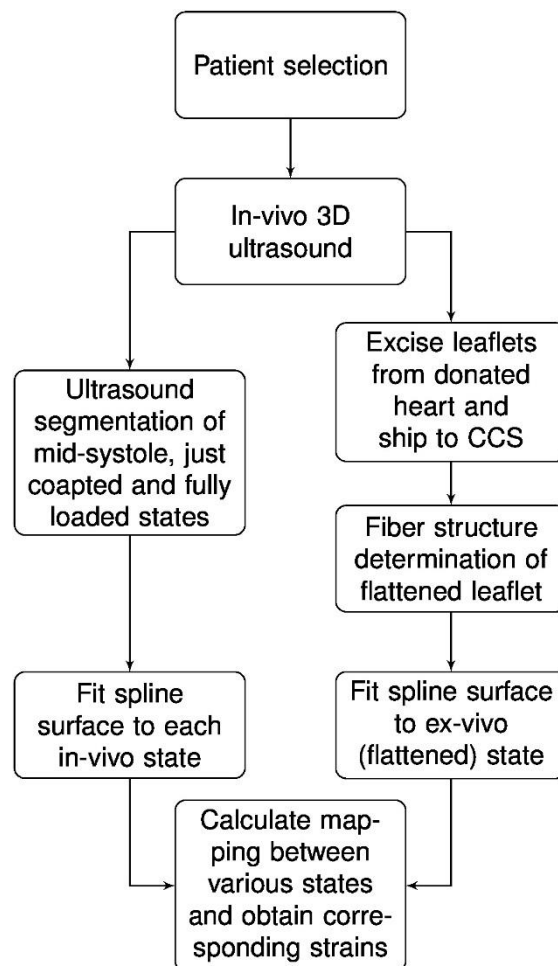
Bibliography

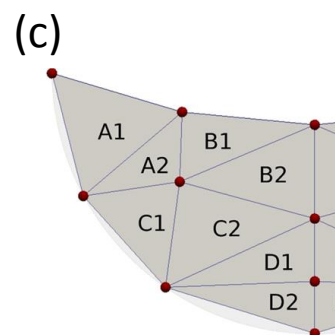
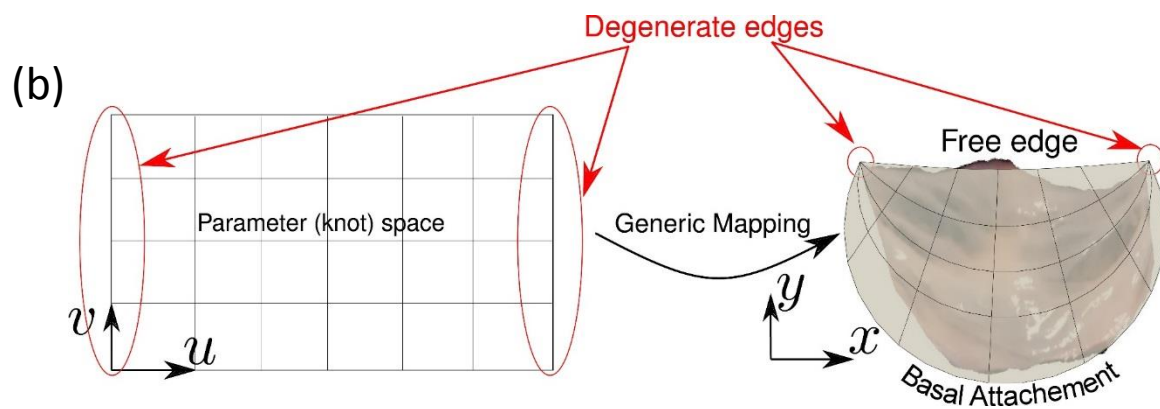
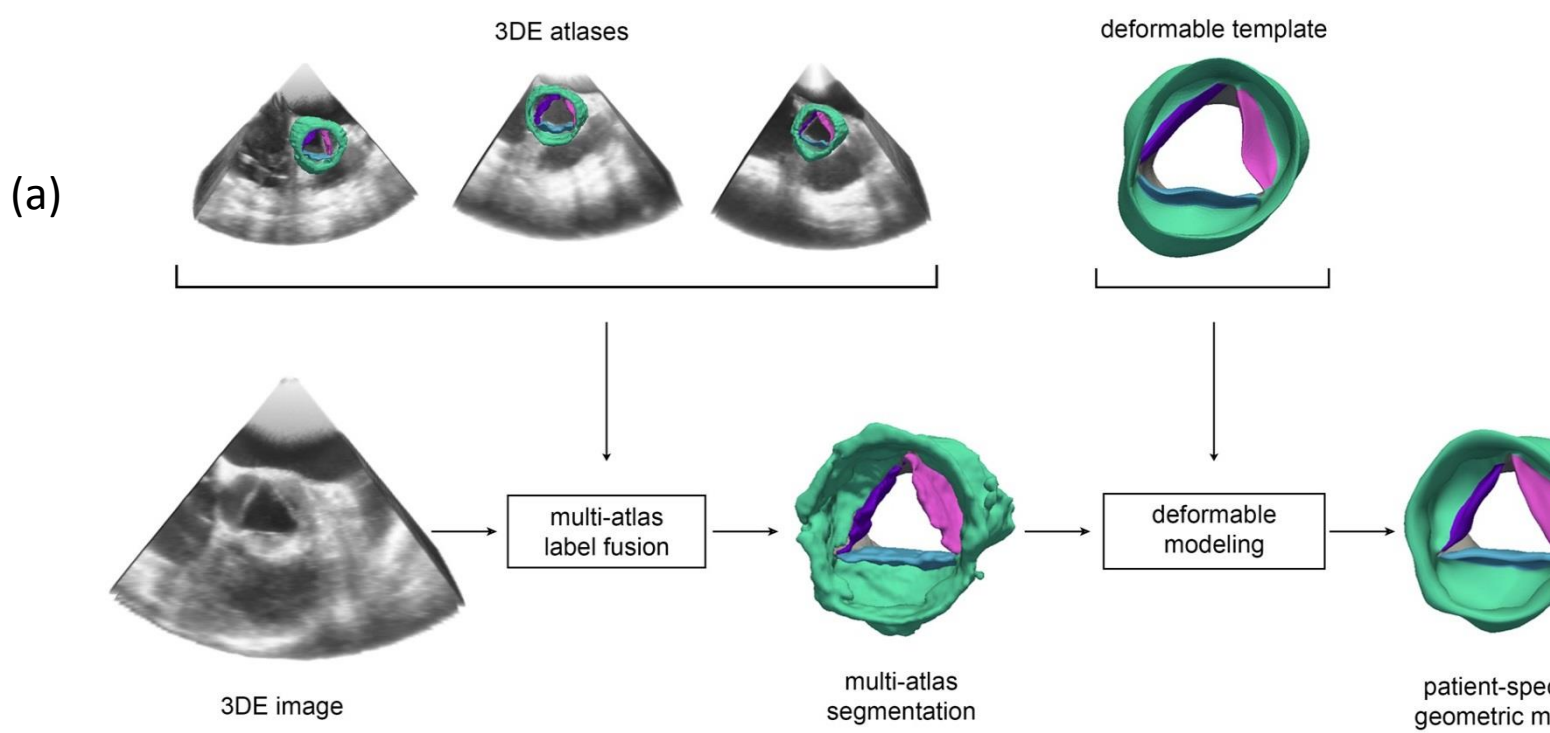
- Adamczyk, M.M., Lee, T.C., Vesely, I., 2000. Biaxial strain properties of elastase-digested porcine aortic valves. *J Heart Valve Dis* 9, 445-453.
- Aggarwal, A., Aguilar, V.S., Lee, C.-H., Ferrari, G., Gorman, J.H., Gorman, R.C., Sacks, M.S., 2013. Patient-specific modeling of heart valves: from image to simulation, *Functional Imaging and Modeling of the Heart*. Springer, pp. 141-149.
- Aggarwal, A., Ferrari, G., Joyce, E., Daniels, M.J., Sainger, R., Gorman, J.H., 3rd, Gorman, R., Sacks, M.S., 2014. Architectural trends in the human normal and bicuspid aortic valve leaflet and its relevance to valve disease. *Ann Biomed Eng* 42, 986-998.
- Aggarwal, A., Sacks, M.S., 2015a. A Framework for Determination of Heart Valves' Mechanical Properties Using Inverse-Modeling Approach. *Functional Imaging and Modeling of the Heart Lecture Notes in Computer Science* 9126, 285-294.
- Aggarwal, A., Sacks, M.S., 2015b. An inverse modeling approach for semilunar heart valve leaflet mechanics: exploitation of tissue structure. *Biomechanics and modeling in mechanobiology*, 1-24.
- Amini, R., Eckert, C.E., Koomalsingh, K., McGarvey, J., Minakawa, M., Gorman, J.H., Gorman, R.C., Sacks, M.S., 2012. On the in vivo deformation of the mitral valve anterior leaflet: effects of annular geometry and referential configuration. *Ann Biomed Eng* 40, 1455-1467.
- Avants, B.B., Epstein, C.L., Grossman, M., Gee, J.C., 2008. Symmetric diffeomorphic image registration with cross-correlation: evaluating automated labeling of elderly and neurodegenerative brain. *Med Image Anal* 12, 26-41.
- Chuong, C.J., Fung, Y.C., 1986a. On Residual Stress in Arteries. *Journal of Biomechanical Engineering* 108, 189-192.
- Chuong, C.J., Fung, Y.C., 1986b. Residual Stress in Arteries, in: Schmid-Schonbein, G., Woo, S.L.Y., Zweifach, B. (Eds.), *Frontiers in Biomechanics*. Springer-Verlag, New York, pp. 117-129.

- Doehring, T.C., Kahelin, M., Vesely, I., 2005. Mesostructures of the aortic valve. *J Heart Valve Dis* 14, 679-686.
- Fung, Y.C., 1991. What are the residual stresses doing in our blood vessels? *Ann Biomed Eng* 19, 237-249.
- Gower, A.L., Ciarletta, P., Destrade, M., 2015. Initial Stress Symmetry and Applications in Elasticity. arXiv preprint arXiv:1506.05038.
- Hongzhi, W., Suh, J.W., Das, S.R., Pluta, J.B., Craige, C., Yushkevich, P.A., 2013. Multi-Atlas Segmentation with Joint Label Fusion. *IEEE Trans Pattern Anal Mach Intell* 35, 611-623.
- Jassar, A.S., Levack, M.M., Solorzano, R.D., Pouch, A.M., Ferrari, G., Cheung, A.T., Ferrari, V.A., Gorman, J.H., 3rd, Gorman, R.C., Jackson, B.M., 2014. Feasibility of in vivo human aortic valve modeling using real-time three-dimensional echocardiography. *Ann Thorac Surg* 97, 1255-1258.
- Johnson, B.E., Hoger, A., 1995. The use of a virtual configuration in formulating constitutive equations for residually stressed elastic materials. *J Elasticity* 41, 177-215.
- Krishnamurthy, G., Ennis, D.B., Itoh, A., Bothe, W., Swanson, J.C., Karlsson, M., Kuhl, E., Miller, D.C., Ingels, N.B., Jr., 2008. Material properties of the ovine mitral valve anterior leaflet in vivo from inverse finite element analysis. *Am J Physiol Heart Circ Physiol* 295, H1141-H1149.
- Lee, C.-H., Sacks, M.S., 2014. Simulation of the layer-specific deformations of mitral valve interstitial cells under physiological loading. *J.Theor.Biol.*
- Lee, C.H., Carruthers, C.A., Ayoub, S., Gorman, R.C., Gorman, J.H., 3rd, Sacks, M.S., 2015. Quantification and simulation of layer-specific mitral valve interstitial cells deformation under physiological loading. *J Theor Biol.*
- Lu, J., 2012. A covariant constitutive theory for anisotropic hyperelastic solids with initial strains. *Mathematics and Mechanics of Solids* 17, 104-119.
- Lu, J., Zhou, X., Raghavan, M.L., 2007. Inverse elastostatic stress analysis in pre-deformed biological structures: Demonstration using abdominal aortic aneurysms. *J Biomech* 40, 693-696.

- Pouch, A.M., Jackson, B.M., Yushkevich, P.A., Gorman, J.H., 3rd, Gorman, R.C., 2015a. 4D-transesophageal echocardiography and emerging imaging modalities for guiding mitral valve repair. *Ann Cardiothorac Surg* 4, 461-462.
- Pouch, A.M., Tian, S., Takabe, M., Wang, H., Yuan, J., Cheung, A.T., Jackson, B.M., Gorman, J.H., 3rd, Gorman, R.C., Yushkevich, P.A., 2015b. Segmentation of the Aortic Valve Apparatus in 3D Echocardiographic Images: Deformable Modeling of a Branching Medial Structure. *Stat Atlases Comput Models Heart* 8896, 196-203.
- Pouch, A.M., Tian, S., Takebe, M., Yuan, J., Gorman, R., Jr., Cheung, A.T., Wang, H., Jackson, B.M., Gorman, J.H., 3rd, Gorman, R.C., Yushkevich, P.A., 2015c. Medially constrained deformable modeling for segmentation of branching medial structures: Application to aortic valve segmentation and morphometry. *Med Image Anal* 26, 217-231.
- Pouch, A.M., Wang, H., Takabe, M., Jackson, B.M., Sehgal, C.M., Gorman, J.H., 3rd, Gorman, R.C., Yushkevich, P.A., 2013. Automated segmentation and geometrical modeling of the tricuspid aortic valve in 3D echocardiographic images. *Medical image computing and computer-assisted intervention : MICCAI ... International Conference on Medical Image Computing and Computer-Assisted Intervention* 16, 485-492.
- Rajagopal, V., Chung, J.H., Bullivant, D., Nielsen, P.M.F., Nash, M.P., 2007. Determining the finite elasticity reference state from a loaded configuration. *International Journal for Numerical Methods in Engineering* 72, 1434-1451.
- Rausch, M.K., Famaey, N., Shultz, T.O., Bothe, W., Miller, D.C., Kuhl, E., 2013. Mechanics of the mitral valve: a critical review, an in vivo parameter identification, and the effect of prestrain. *Biomech Model Mechanobiol* 12, 1053-1071.
- Rausch, M.K., Kuhl, E., 2013. On the effect of prestrain and residual stress in thin biological membranes. *J Mech Phys Solids* 61, 1955-1969.

- Sacks, M.S., Lam, T.V., Mayer, J.E., Jr., 2004. A structural constitutive model for the native pulmonary valve. *Conf Proc IEEE Eng Med Biol Soc* 5, 3734-3736.
- Sacks, M.S., Merryman, W.D., Schmidt, D.E., 2009. On the biomechanics of heart valve function. *J Biomech* 42, 1804-1824.
- Sacks, M.S., Smith, D.B., Hiester, E.D., 1997. A small angle light scattering device for planar connective tissue microstructural analysis. *Ann Biomed Eng* 25, 678-689.
- Squillacote, A.H., *The ParaView Guide: A Parallel Visualization Application*. Kitware Inc., 2007. ISBN 1-930934-21-1.
- Stella, J.A., Sacks, M.S., 2007. On the biaxial mechanical properties of the layers of the aortic valve leaflet. *J Biomech Eng* 129, 757-766.
- Vesely, I., Lozon, A., Talman, E., 1993. Is zero-pressure fixation of bioprosthetic valves truly stress free? *Journal of Thoracic Cardiovascular Surgery* 106, 288-298.
- Vesely, I., Noseworthy, R., 1992. Micromechanics of the fibrosa and the ventricularis in aortic valve leaflets. *Journal of Biomechanics* 25, 101-113.
- Weiler, M., Yap, C.H., Balachandran, K., Padala, M., Yoganathan, A.P., 2011. Regional analysis of dynamic deformation characteristics of native aortic valve leaflets. *J Biomech* 44, 1459-1465.
- Witschey, W.R., Pouch, A.M., McGarvey, J.R., Ikeuchi, K., Contijoch, F., Levack, M.M., Yushkevich, P.A., Sehgal, C.M., Jackson, B.M., Gorman, R.C., Gorman, J.H., 3rd, 2014. Three-dimensional ultrasound-derived physical mitral valve modeling. *Ann Thorac Surg* 98, 691-694.
- Yushkevich, P.A., Piven, J., Hazlett, H.C., Smith, R.G., Ho, S., Gee, J.C., Gerig, G., 2006a. User-guided 3D active contour segmentation of anatomical structures: significantly improved efficiency and reliability. *Neuroimage* 31, 1116-1128.
- Yushkevich, P.A., Zhang, H., Gee, J.C., 2006b. Continuous medial representation for anatomical structures. *IEEE Trans Med Imaging* 25, 1547-1564.



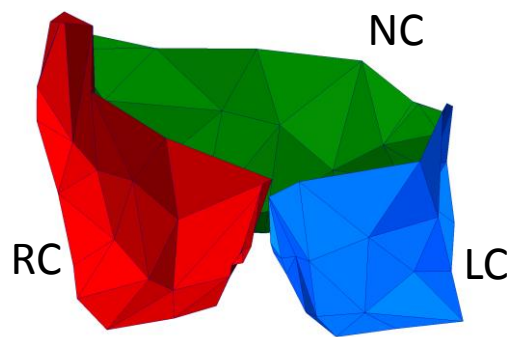


Open (mid-systole) state

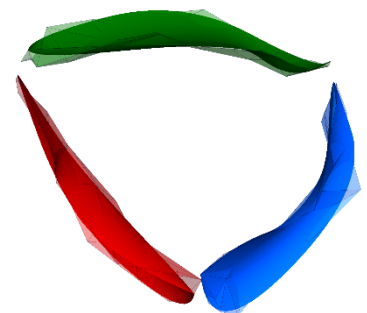
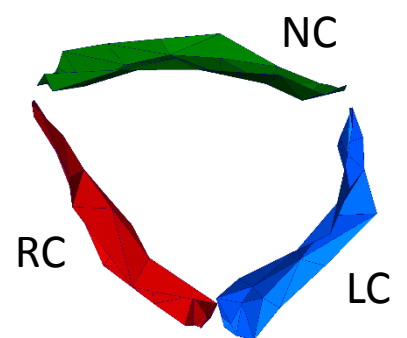
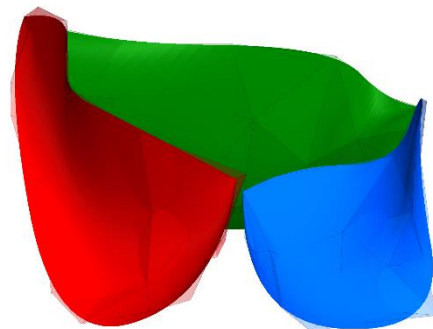
3DE



Segmentations



Spline fits

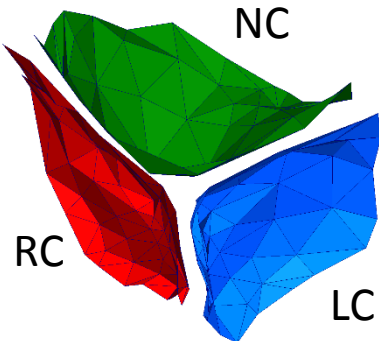


Fully loaded state

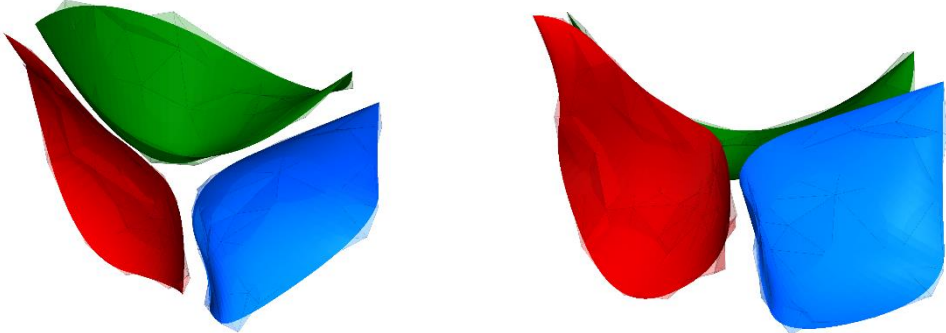
3DE

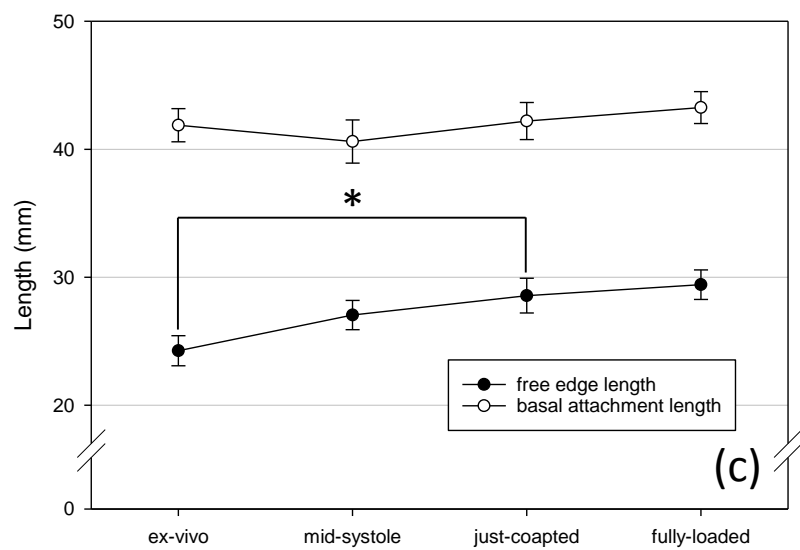
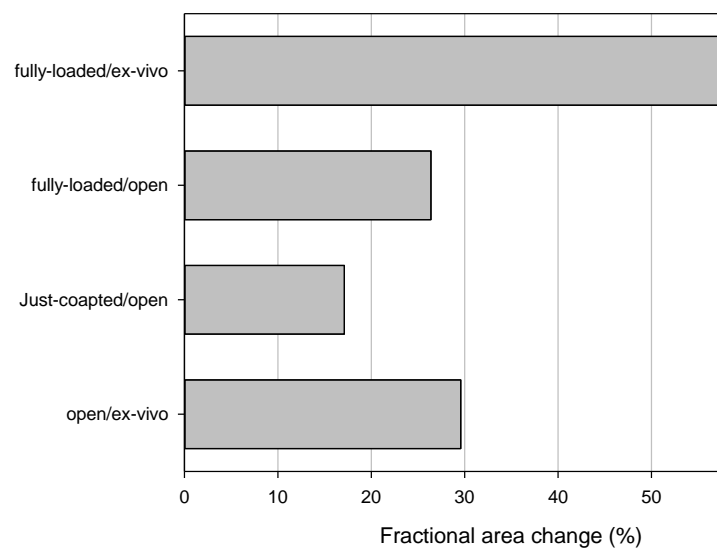
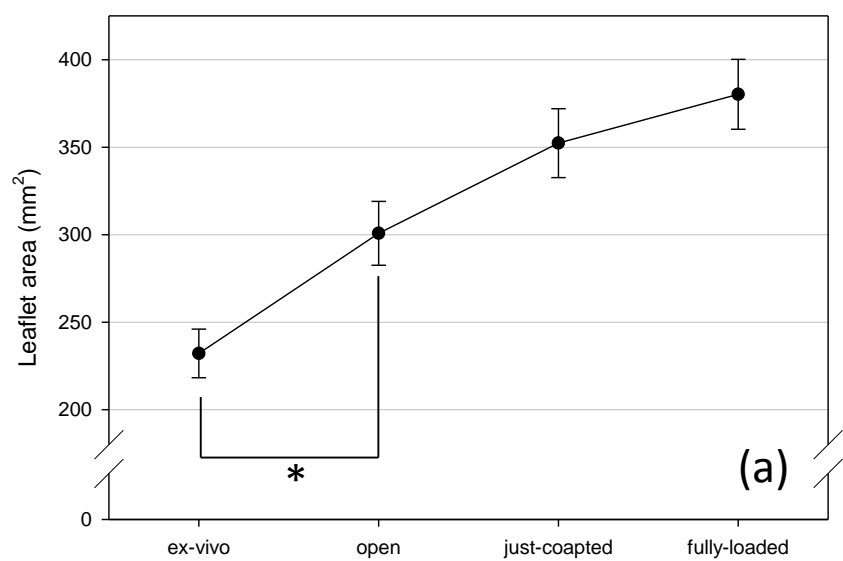


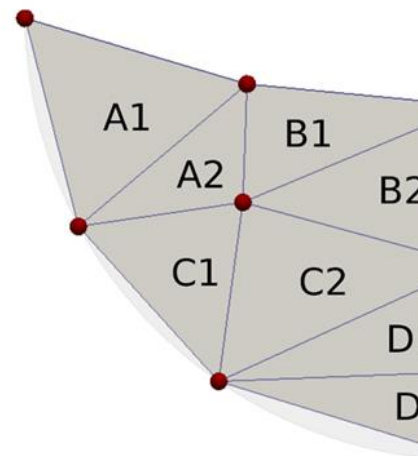
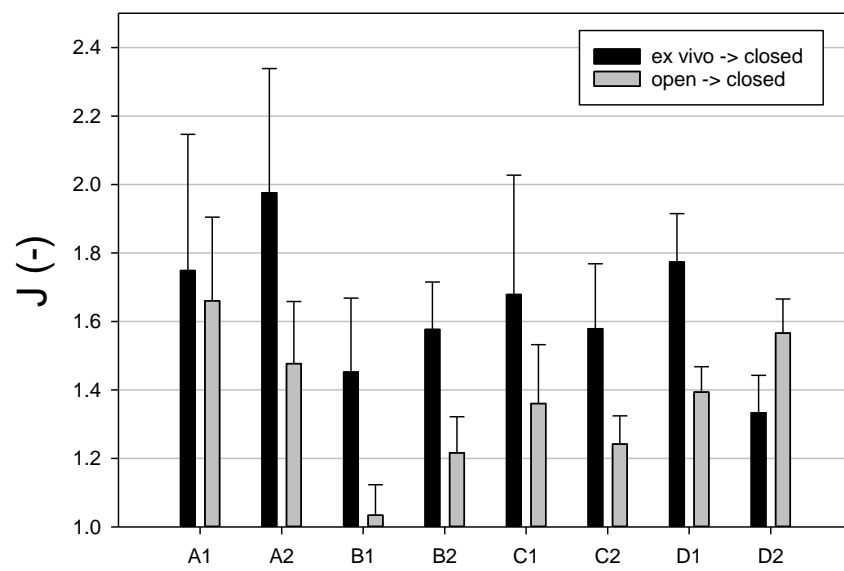
Segmentations



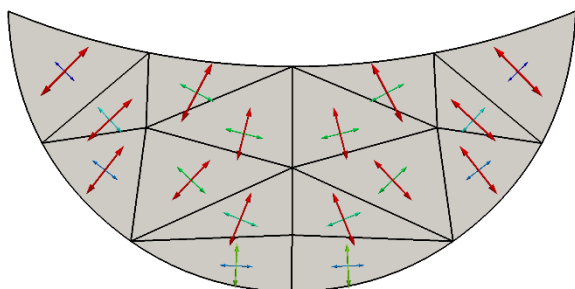
Spline fits



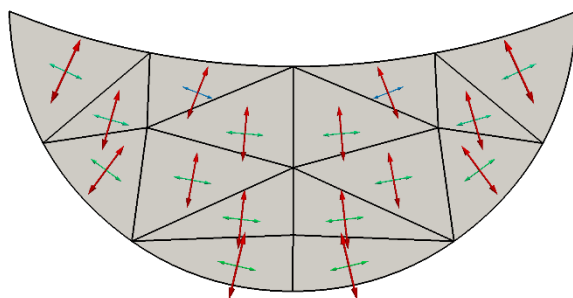




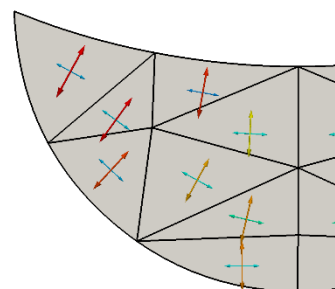
Ex-vivo to in-vivo (open)



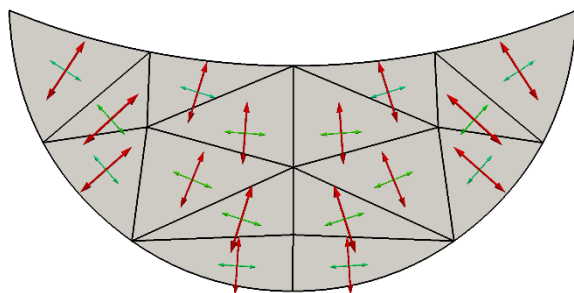
Open to just-coapted



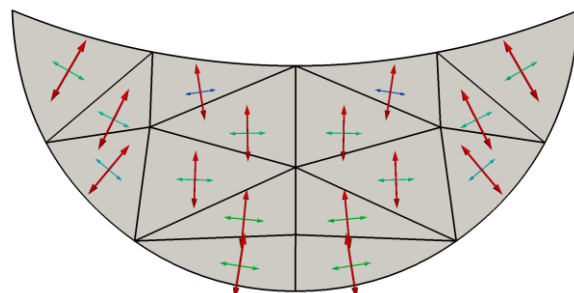
Just-coapted
fully-loaded

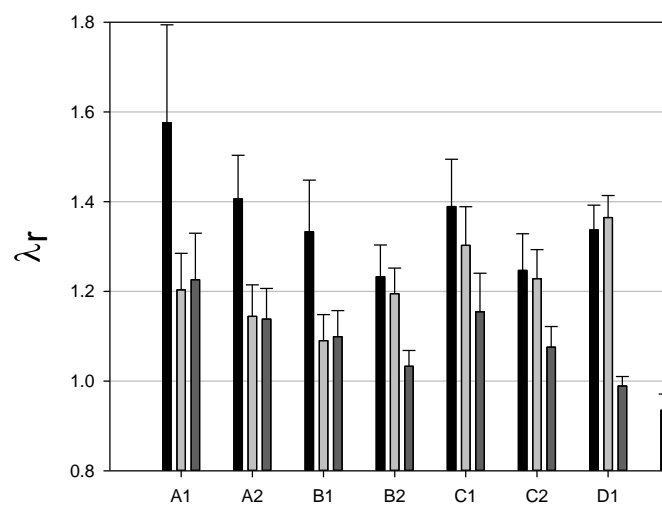
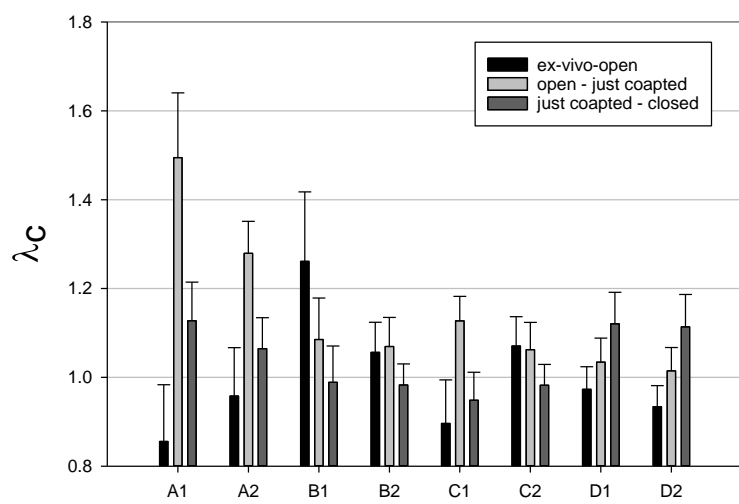


Ex-vivo to fully-loaded

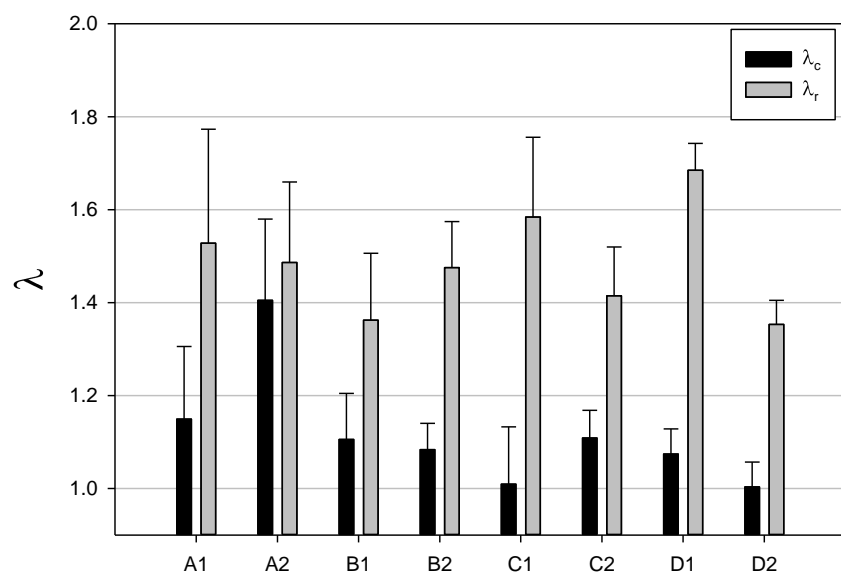


Open to fully-loaded





ex-vivo to closed



open to closed

